



UNIVERSITY OF
PLYMOUTH



School of Geography, Earth and Environmental Sciences
Faculty of Science and Engineering

2024-08-02

Pathways and timescales of Southern Ocean hydrothermal iron and manganese transport

Antony J. Birchill *Environment Agency*

Chelsea Baker *National Oceanographic Centre*

Neil Wyatt *University of Plymouth*

Katsiaryna Pabortsava *National Oceanographic Centre*

Hugh Venables *British Antarctic Survey*

et al. *See next page for additional authors*

Let us know how access to this document benefits you

General rights

All content in PEARL is protected by copyright law. Author manuscripts are made available in accordance with publisher policies. Please cite only the published version using the details provided on the item record or document. In the absence of an open licence (e.g. Creative Commons), permissions for further reuse of content should be sought from the publisher or author.

Take down policy

If you believe that this document breaches copyright please [contact the library](#) providing details, and we will remove access to the work immediately and investigate your claim.

Follow this and additional works at: <https://pearl.plymouth.ac.uk/gees-research>

Recommended Citation

Birchill, A., Baker, C., Wyatt, N., Pabortsava, K., Venables, H., Moore, M., Turnbull, I., Milne, A., Ussher, S., Oliver, S., & Martin, A. (2024) 'Pathways and timescales of Southern Ocean hydrothermal iron and manganese transport', *Communications Earth and Environment*, 5(1). Available at: <https://doi.org/10.1038/s43247-024-01564-8>

This Article is brought to you for free and open access by the Faculty of Science and Engineering at PEARL. It has been accepted for inclusion in School of Geography, Earth and Environmental Sciences by an authorized administrator of PEARL. For more information, please contact openresearch@plymouth.ac.uk.

Authors

Antony J. Birchill, Chelsea Baker, Neil Wyatt, Katsiaryna Pabortsava, Hugh Venables, Mark Moore, Isobel Turnbull, Angela Milne, Simon Ussher, Sophy Oliver, and Adrian Martin



PEARL

Pathways and timescales of Southern Ocean hydrothermal iron and manganese transport

Birchill, Antony J.; Baker, Chelsea ; Wyatt, Neil; Pabortsava, Katsiaryna; Venables, Hugh; Moore, Mark; Turnbull, Isobel; Milne, Angela; Ussher, Simon; Oliver, Sophy ; Martin, Adrian

Published in:

Communications Earth and Environment

DOI:

[10.1038/s43247-024-01564-8](https://doi.org/10.1038/s43247-024-01564-8)

Publication date:

2024

Document version:

Peer reviewed version

Link:

[Link to publication in PEARL](#)

Citation for published version (APA):

Birchill, A. J., Baker, C., Wyatt, N., Pabortsava, K., Venables, H., Moore, M., Turnbull, I., Milne, A., Ussher, S., Oliver, S., & Martin, A. (2024). Pathways and timescales of Southern Ocean hydrothermal iron and manganese transport. *Communications Earth and Environment*, 5(1), Article 413. <https://doi.org/10.1038/s43247-024-01564-8>

Pathways and timescales of Southern Ocean hydrothermal iron and manganese transport

Antony J. Birchill^{1,2*}, Chelsey A. Baker^{3*}, Neil J. Wyatt^{2,5}, Katsiaryna Pabortsava³, Hugh J. Venables⁴, C. Mark Moore⁵, Isobel Turnbull², Angela Milne², Simon J. Ussher², Sophy Oliver³ and Adrian P. Martin³

¹ Chief Scientist's Group, Environment Agency, Romsey District Office, SO51 7LP, UK.

² School of Geography, Earth and Environmental Sciences, Plymouth University, Drake Circus, Devon, PL4 8AA, UK.

³ National Oceanography Centre, European Way, Southampton, SO14 3ZH, UK.

⁴ Polar Oceans Team, British Antarctic Survey, High Cross, Madingley Road, Cambridge, CB3 0ET, UK.

⁵ School of Ocean and Earth Sciences, University of Southampton, Waterfront Campus, National Oceanography Centre, European Way, SO14 3ZH, UK.

*lead co-authors who contributed equally to the work

Author contributions: AJB and CAB wrote the initial draft and all co-authors contributed to draft revisions. AJB, CAB, NJW, KP, HJV, CMM, IT, AM, SJU and APM participated in the field campaign. AJB and NJW conducted trace metal (micronutrient) analysis. KP performed macronutrient analysis. HJV processed conductivity-temperature-depth sensor package datasets. CAB performed Lagrangian modelling experiments and analysis. SO carried out the water mass analysis. APM, CMM, SJU and AM wrote and planned the original research questions and funding proposal. APM led the research program. The views expressed in this paper are those of the authors alone, and not the organisations for which they work.

22 **Abstract**

23 Scarcity of iron (Fe) and manganese (Mn) limits the efficiency of the biological carbon pump over large
24 areas of the Southern Ocean (SO). The importance of hydrothermal vents as a source of these
25 micronutrients to the euphotic zone of the SO is debated. We present full depth profiles of dissolved
26 and total dissolvable trace metals in the remote eastern Pacific sector of the SO (55-60°S, 89.1°W),
27 providing evidence of enrichment of Fe and Mn at depths of 2000-4000 m. These enhanced
28 micronutrient concentrations were co-located with ³He enrichment, an indicator of hydrothermal fluid
29 originating from ocean ridges. Modelled water trajectories revealed the understudied South East Pacific
30 Rise and the Pacific Antarctic Ridge as likely source regions. Additionally, the trajectories demonstrate
31 pathways for these SO hydrothermal ridge-derived trace metals to reach the SO surface mixed layer
32 within two decades, potentially supporting a regular supply of micronutrients to fuel SO primary
33 production.

1.0 Introduction

Despite being the largest high-nutrient low-chlorophyll region^{1,2}, the Southern Ocean (SO) is a globally important organic carbon sink, with the interplay between circulation and remineralisation dynamics setting the rate of carbon uptake by the biological carbon pump³ and 10% of global biological carbon export occurring in the region⁴. Iron (Fe) is an essential but often scarce micronutrient that can limit primary production and the efficiency of the biological carbon pump in the SO^{5,6}. However, other elements can potentially be (co-)limiting alongside Fe in the Southern Ocean (SO)⁷, with recent evidence for manganese (Mn) (co-)limitation in particular^{2,8–10}.

As non-conservative elements with residence times on the order of decades in the deep ocean¹¹, the distributions of dissolved Fe and Mn (dFe, dMn; <0.2 μm) in seawater are spatially coupled to sources. The main external sources of Fe and Mn to the ocean are margin sediments, atmospheric dust, and hydrothermal venting^{6,12}. Input from margin sediments enhances primary production downstream of islands in the SO^{13,14}, and sustains ecosystems in Antarctic shelf regions^{12,15}, where melting glacial ice can be an additional source of Fe and Mn^{16,17}. Marine aerosol Fe concentrations can vary by >3 orders of magnitude, causing sporadic and seasonal changes to the widespread deposition of Fe to the surface ocean¹⁸. However, according to both observations and models, the remote southern hemisphere oceanic gyres and polar regions have some of the lowest Fe aerosol deposition fluxes in the world (<0.01 g Fe m⁻² yr⁻¹)¹⁹.

Both Fe and Mn are concentrated in hydrothermal fluids, often enriched by a factor of >10⁶ relative to background seawater²⁰. Early studies suggested that Fe and Mn entering the ocean from hydrothermal vents was precipitated or scavenged and sedimented close to vent sites^{12,21}, with precipitation reported to occur before the plume reaches neutral buoyancy²². However, it is now known that a small, but significant, fraction of the dFe supplied from hydrothermal vents is sufficiently stabilised against precipitation to be transported in the ocean interior^{23–25}. Hydrothermal venting is

estimated to supply 4 ± 1 Gmoles dFe yr⁻¹ to the wider deep ocean away from the proximal vent sites^{23,26}, representing a continuous Fe input in contrast to short term variations observed in other Fe sources, such as atmospheric deposition²⁶. Similarly, observed increases in deep ocean dMn concentrations have been attributed to hydrothermal activity¹⁶, and incorporating hydrothermal dMn inputs increases the accuracy of modelled oceanic dMn distributions¹². Our understanding of the hydrothermal plume processes responsible for the physico-chemical stabilisation of Fe is developing, though not yet comprehensive. Within hydrothermal plumes dFe has been shown to form inorganic nanoparticles^{27,28}, larger inorganic colloids²⁹ and organic complexes^{30,31}. The co-location of carbon with Fe in plume particles suggests that organic carbon may alter the chemical behaviour of Fe oxyhydroxides²⁹ and create localised regions of Fe(II) enrichment³¹.

Due to the inhibition of vertical mixing in the ocean interior by density stratification, hydrothermal plumes tend to travel predominantly along isopycnals^{32,33}. Westerly winds drive the Antarctic Circumpolar Current (ACC) to create a northward surface flow (Ekman Transport), causing isopycnals to shoal in the SO³⁴. Consequently, upwelling deep waters in the SO may provide a pathway for hydrothermal trace metals to be mixed into the SO euphotic zone^{21,35}. Inputs of hydrothermal dFe from shallow (<500m) and deep (>2000m) vents have been linked to regional phytoplankton blooms within^{36,37} and outside of the SO³⁸. The potential for hydrothermal dFe to sustain primary production in the SO has been evaluated in models^{39,40}, but consensus on the significance of this source of Fe and Mn has yet to be reached.

To sustain SO primary production, upwelling timescales must be short enough to deliver hydrothermal Fe and Mn to the euphotic zone before removal processes, such as scavenging and precipitation, deplete these metals. Assuming that some degree of physicochemical stabilisation of dFe in neutrally buoyant plumes may allow transportation to surface waters, model results indicate that hydrothermal Fe could support ≈ 15 -30% of export production south of the Polar Front^{39,41}. However,

estimates of dFe residence time in the East Pacific Rise (EPR) far field plume at 15°S have been revised from quasi-conservative, based on comparisons with ^3He measurements²³, to non-conservative with a residence time of 9-50 years, based on comparisons with ^{228}Ra measurements⁴². The 9-50 year residence time estimate is consistent with a global modelling study estimate of hydrothermal Fe residence time of 21-35 years³⁹. Similarly, deep ocean dMn residence times are estimated at 5-40 years¹¹.

In comparison, transit time estimates for the shoaling of Circumpolar Deep Waters (CDW), originating in the Pacific ($\geq 30^\circ\text{S}$), to the SO mixed layer range from 17 years to a few centuries^{43–46}. Such uncertainty surrounding hydrothermal Fe input and stabilisation processes, alongside SO ventilation rates, is reflected in Fe modelling studies. A global steady state inverse circulation model combined with a mechanistic Fe model was used to conclude that only 3-5% of hydrothermal dFe reaches surface waters globally⁴⁰. A subsequent study argued however that the inverse modelling approach reduces the magnitude of hydrothermal Fe inputs from ridge systems located within the SO relative to a spreading rate model approach³⁹. This ongoing debate is hindered by a lack of observational evidence of the key transport pathways. The Southeast Pacific sector of the SO has been indicated as a critical region for hydrothermal Fe and Mn input by models^{12,39}, but is a ‘data desert’ for trace metal observations. In this study, we provide the first full depth profiles of Fe and Mn from this SO region, which show a clear midwater hydrothermal trace metal signal. By modelling water pathways, we trace the hydrothermal signal back to specific ridge systems and evaluate whether the observed hydrothermal Fe and Mn could supply the SO mixed layer, and therefore fuel SO primary production.

2.0 Results and Discussion

2.1 Observations of hydrothermal trace metals in the southeast Pacific sector of the Southern Ocean

Our study sampled a north-south transect along 89°W located in the Mornington Abyssal Plain (MAP) in the southeast Pacific Ocean (Fig. 1 A). As expected, SO surface waters were characterised by extremely low dFe (<0.2 µM, 0-30 m depth; 0.09 ± 0.04 nM, $n=18$) and total dissolvable Fe (TdFe; unfiltered) concentrations (0-30 m depth; 0.19 ± 0.09 nM, $n=13$; Fig. 1B, C) and excess macronutrient concentrations (nitrate + nitrite 16.6-23.6 µM, phosphate 1.0-1.6 µM; data not shown), consistent with previous upper ocean observations in this region⁴⁷ and wider SO biogeochemistry³⁵.

The most striking feature of our transect was Fe enrichment in deep waters (Fig. 1B, C), with dFe concentrations of 0.48 to 0.96 nM occurring between 2000-4000 m at the northern end of our transect (Ocean Observatories Initiative (OOI) sustained observatory location, 54.08°S 89.67°W <https://oceanobservatories.org/array/global-southern-ocean-array/> ; Fig. 1A, Table S1). Higher TdFe concentrations (>2.5 nM with a maximum concentration of 15.4 nM), associated with lower dFe concentrations, were also observed in benthic nepheloid layers driven by particle accumulation and benthic sediment resuspension of particulate Fe and scavenging of dFe (Fig. 1C, Fig 2D.). For comparison, high particulate Fe concentrations (up to 88 nM) were observed above the seafloor at open ocean stations in the north Atlantic⁴⁸.

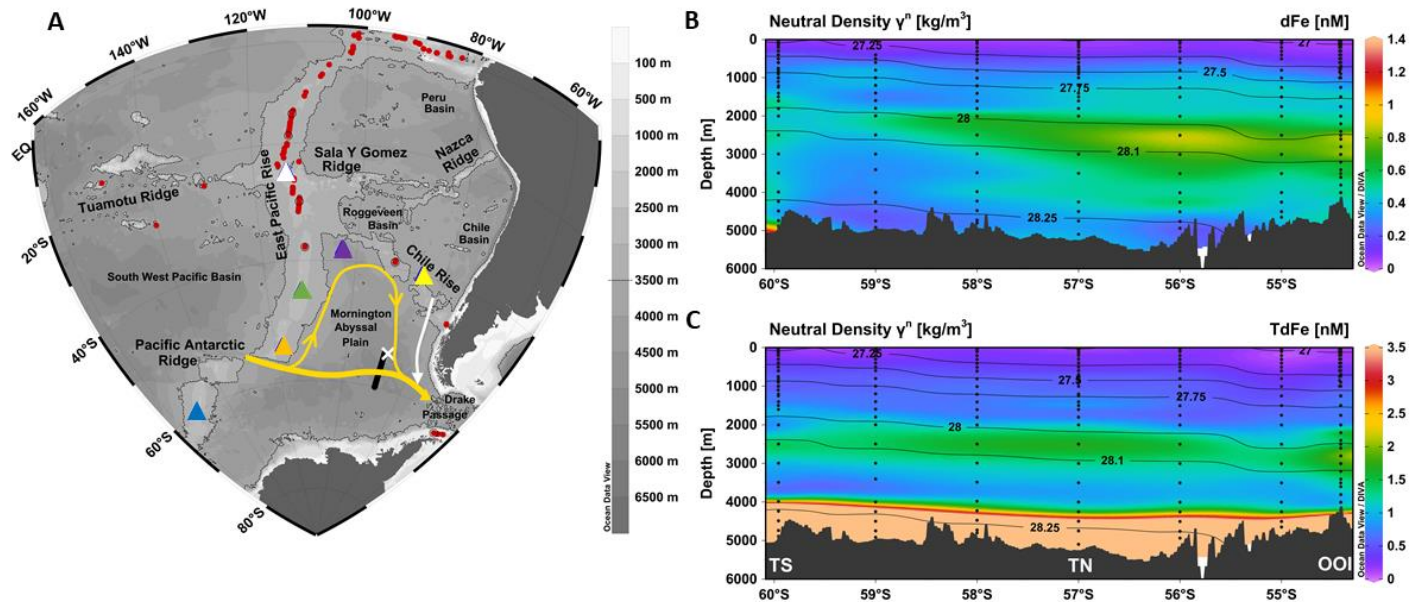


Figure 1. **A** Study area in the southeast Pacific and Southern Ocean. Red dots are the location of known active vent sites⁴⁹. Lack of exploration means that knowledge of active vent site locations over the region is incomplete. The yellow arrow is the approximate flow of water at 2000-4000 m depth⁵⁰ and white arrow the approximate flow of Southeast Pacific Deep Slope Water⁵¹. The solid black line is the transect occupied by this study. The white cross is the sampling location of a previous ³He profile⁵² collected in 1993 approximately 83 km northeast (bearing of 055°) of our northernmost station. Triangles indicate the start locations for forward-tracked trajectory modelling in this study: yellow - East Chile Rise, purple – West Chile Rise, white – Easter Microplate, green – North East Pacific Rise, orange – South East Pacific Rise (SEPR) and blue – Pacific Antarctic Ridge (PAR). **B** and **C** are section plots of dFe (<0.2 μm) and TdFe (unfiltered) concentrations along the transect with neutral density overlain. Black dots mark sampling depths. Note that concentrations in **B** and **C** are on different scales and that TdFe concentrations were typically >2.5 nM near the seafloor. The maximum concentration measured was 15.39 ± 1.12 nM. OOI is the sampling location coinciding with the Ocean Observatories Initiative mooring. Stations OOI, TN and TS (panel C) are the locations of trace metal depth profiles displayed in Figure 2.

Away from external sources, deep ocean dMn concentrations are typically very low (<0.2 nM) due to scavenging removal into the particulate phase and oxidation of Mn ions to insoluble Mn oxides¹⁶. However, like dFe, basin-scale transport in vent plumes has been observed e.g. westward transport of dMn from the EPR (10 - 17° S) occurs in the low latitude Pacific Ocean²³. Along our transect we present, elevated dMn concentrations (up to 0.39 nM, Table S1) occurred coincidently with the enriched dFe signal (Fig. 2A, B and C), compared to a background dMn concentration (~ 0.2 nM) immediately above and below the mid-depth enrichment (Fig. 2B and C). In the southwest Pacific (170° W), CDW has background dMn concentrations of ~ 0.1 - 0.2 nM⁵³ away from hydrothermal and sediment inputs. The Fe and Mn enrichment we observed was centered on a neutral density surface of $\gamma_n = 28.0$ - 28.1 kg m⁻³ (Fig. 2D), within CDW (Fig. S1). This density surface shoals by ~ 880 m towards the south of the transect as part of the wider Ekman driven upwelling occurring in the SO. The influence of this wind-driven upwelling is shown clearly in the maximum dFe concentrations, which tracked the isopycnals along the depth section (Fig. 1) and in the dMn profiles from stations OOI, TN and TS (Fig. 1B, C and Fig. 2A and B, Table S1).

Mantle helium (He), which is enriched in primordial ^3He , is also released into the ocean at mid-ocean ridges. A ratio of $^3\text{He}/^4\text{He}$ in excess of atmospheric values (hereafter $x\text{s}^3\text{He}$) in deep ocean waters is a widely used tracer of hydrothermal inputs⁵². Tagliabue et al. (2022) indicated that the basin-scale hydrothermal Fe supply from SO vents is not well predicted by the spatial distribution of ^3He inputs, likely because of inter-vent Fe: ^3He ratio variability. Nevertheless, at a single location the coincident enrichment of ^3He , Fe and Mn in deep ocean waters is indicative of hydrothermal input of these elements. Helium isotope observations, previously sampled near station OOI (Fig. 1), revealed the presence of $x\text{s}^3\text{He}$ at the depths and neutral density of our observations of trace metal enrichment (Fig. 2 C,D). Although the helium dataset 26 years, and 83 km away from our trace metal observations, the comparable distribution of dFe, TdFe and $x\text{s}^3\text{He}$ with neutral density (Fig. 2D) provides confidence that

we observed a consistent oceanographic signal in both datasets. However, we cannot account for any temporal variability of end-member metal and helium concentrations during the 26-year gap between trace metal and helium sample collection⁵⁴. The Fe concentration maximum at the northern end of our study site was slightly deeper (215 m) than the mantle xs^3He maximum. A similar offset in the distribution has been observed further north in the far field plume of the EPR (20-26°S) and has been attributed to reversible scavenging of dFe onto sinking particles, which deepens the metal concentration maximum⁵⁵. The offset we observed may also be due to temporal variability of end member metal and helium concentrations, the influence of multiple vent sites with varying Fe: ^3He ratios, and/or reversible scavenging combined with layering of fine particulate material with irregular element distribution within plumes⁴¹.

The balance between the release of dFe from remineralising organic matter and removal of dFe from solution via scavenging processes leads to an accumulation of dFe in Pacific Mode and Intermediate Waters⁵⁶. We show that the signal we observed is decoupled from the mineralization of biogenic particles by plotting dFe against apparent oxygen utilisation (AOU; Fig. S2). In waters below the mixed layer there is a positive linear relationship between dFe and AOU indicating that remineralisation of sinking organic matter exerts an important control on dFe concentrations, consistent with previous investigations of Pacific mode and intermediate waters⁵⁶. However, the enrichment of dFe we observe in deeper waters clearly deviates from the linear dFe-AOU trend indicating an additional deep water dFe source such as long range transport of hydrothermal dFe²⁴

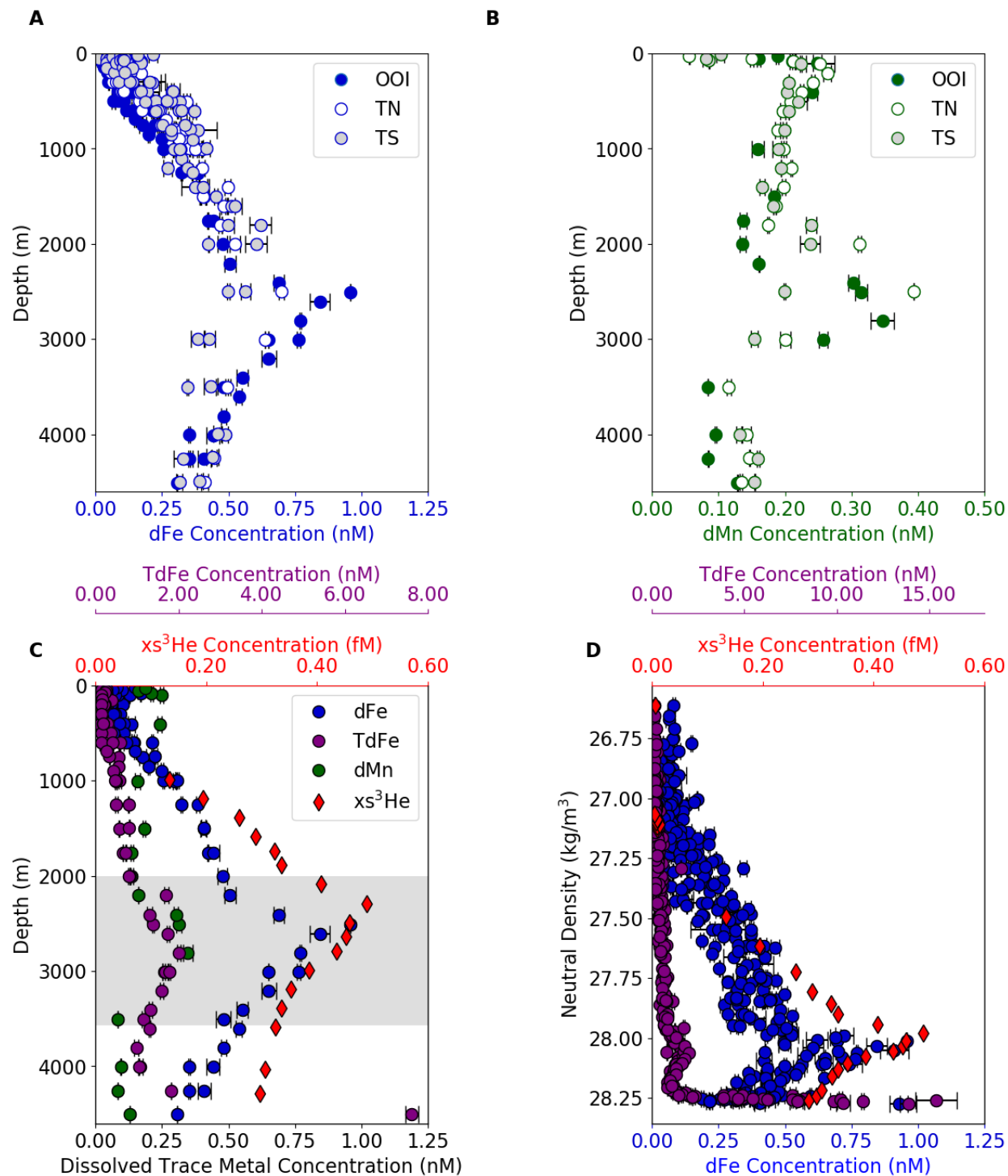


Figure 2. A Depth profiles of dFe at stations OOI, TN and TS. **B** Depth profiles of dMn at stations OOI, TN and TS. **C** Depth profiles of dissolved trace metals (dFe and dMn) and TdFe at our northernmost station

OOI (combined Fe data from 4 site visits) and nearby historic xs^3He (see Fig. 1A; white cross). **B** All dFe and TdFe data from the transect and nearby historic xs^3He plotted against neutral density.

2.2 Identifying the source region of the observed hydrothermal signal

The bathymetry of the southeast Pacific Ocean has several mid-ocean ridge systems (Fig. 1A), the most prominent being the EPR which is aligned meridionally at $\sim 115^\circ W$ at depths of around 2500 m. The southern extension of the EPR, the Pacific Antarctic Ridge (PAR), is aligned zonally ($\sim 55-65^\circ S$). The Chile Rise ($\sim 40-45^\circ S$) bounds the North of the Mornington Abyssal Plain (MAP; our study region) between the EPR and the coast of Chile. The OOI site is a little south of the confluence of the easterly flowing ACC and the eastern boundary current. The latter flows within ~ 1500 km of the coast of South America between 1500 m and 3500 m, this Southeast Pacific Deep Slope Water⁵¹ represents the main route for mid-depth flow in the South Pacific to enter the SO^{51,57,58}. Volcanic activity at multiple sites along ridge systems (Fig. 1A), alongside complex interior circulation, results in widespread xs^3He in intermediate and deep waters ($\sim 1000-4000$ m) in the South Pacific Ocean⁴⁶. A previous meridional transect along $88^\circ W$ shows the southward extension of xs^3He towards our study area (Fig. S3A), which could indicate plumes originating from ridges to the north e.g., the Sala Y Gomez Ridge and Chile Rise (Fig. 1A). Similarly, a zonal transect along $54^\circ S$ shows an eastward extension of xs^3He from the South EPR (SEPR) that intersects the OOI station (Fig. 3D; Fig. S3B). Because the xs^3He observations do not allow us to discern a clear source region, we undertook trajectory tracking simulations to provide an independent estimate for the origin of the hydrothermal signal.

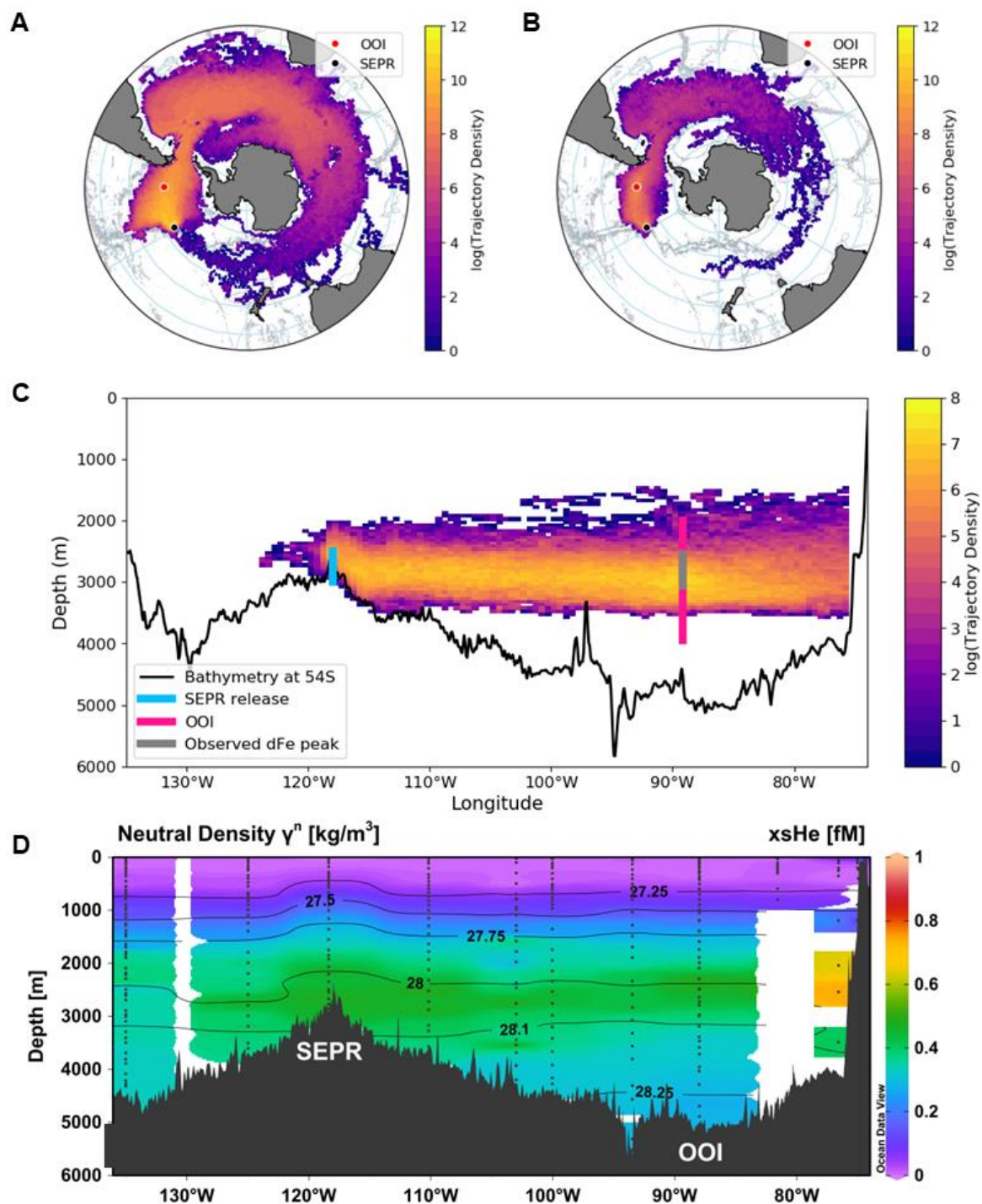
To trace trajectories from potential sources, a series of model release sites were first selected. Along the poorly-explored southern ridge systems, bathymetry along with xs^3He observations and previous literature³³ were used to select an arc of potential release sites to the north and west of station OOI. To simulate a neutrally buoyant hydrothermal plume, trajectories were initiated within a 0.5° grid

around an assumed source extending 500 m upwards in the water column above the ridge at the West Chile Rise (WCR), East Chile Rise (ECR), North EPR (NEPR), South EPR (SEPR) and PAR South (PARS) locations (Fig.1; Table 1) and tracked forwards in time. A reverse simulation was also performed whereby trajectories were backtracked from within a 0.5° grid around the OOI site between 2000-3950 m depth, coincident with our hydrothermal Fe and Mn enrichment observations (Table 1; Fig.2C), towards the ridge systems. The mid-ocean ridge system surrounding our study region was divided into 5 regions (Fig. S4, Table S4), including an additional region PAR North (PARN) which did not have a forward-tracking release site. We quantified the backwards trajectories that passed through the likely plume depths (i.e. extending up to 500 m of water column above a ridge^{59–61}) in these regions (Table 1 and S2). For both forward and backwards tracking, trajectories were traced for 20 years by applying a Lagrangian simulator, called ‘parcels’ (<https://oceanparcels.org/>⁶²), to the velocity components of a global ocean model (Nucleus for European Modelling of the Ocean; NEMO)⁶³ at an eddy-resolving (0.083°) horizontal resolution. Trajectories estimate the flow of water within the model ocean and do not represent concentrations of trace metals.

222 **Table 1.** Summary of trajectory simulations used to identify possible hydrothermal source regions. The proportion of trajectories that passed
 223 within a 0.5° area around the OOI site are presented relative to the number of particles that were successfully released during each simulation
 224 (Table S2 and S3). The source regions that trajectories were tracked backwards in time towards were much larger than the area around station
 225 OOI, as they span along sections of the ridges, allowing more trajectories to pass into the source regions in the backward-tracking simulations
 226 (Table S2, S3 and S4).

Experiment type	Trajectory starting point	Observed signal	Ridge depth (m)	Trajectory seeding depth range (m)	Proportion of trajectories that passed near observed signal (%)	Median first passage time (years from start)
Forward	ECR	OOI	3900	3400-3900	0	>20
Forward	WCR	OOI	3900	3400-3900	0	>20
Forward	SEPR	OOI	3000	2500-3000	9.5	9.8
Forward	NEPR	OOI	3200	2700-3200	0.3	17.9
Forward	PARS	OOI	2800	2300-2800	0.9	15.1
Experiment type	Trajectory starting point	Source region	Ridge depth (m)	Plume source depth range (m)	Proportion of trajectories that passed near potential source (%)	Median first passage time (years from start)
Backward	OOI	ECR/WCR	3900	3400-3900	0	>20
Backward	OOI	SEPR	3000	2500-3000	20.7	11.8
Backward	OOI	NEPR	3200	2700-3200	1.3	14.4
Backward	OOI	PARN	3000	2500-3000	20.3	12.7
Backward	OOI	PARS	2800	2300-2800	7.7	14.4

227



229

230 **Figure 3.** Trajectories of the forward-tracking simulations from the SEPR (A, B, C) and coincident xs^3He

231 anomaly (D). Trajectories were released between the ridge and 500 m above to mimic a neutrally-

buoyant hydrothermal plume. **A** Trajectory density, which indicates the number of instances of trajectories passing into a grid cell (log scale), of all SEPR trajectories. **B** Trajectory density map of SEPR trajectories that pass within a 0.5° area around the OOI station (red marker). **C** Depth section of trajectory density for the SEPR trajectories that pass within a 0.5° area of the OOI station (location indicated by pink line). Additionally, the grey line superimposed on the pink line highlights the depth range where dFe concentrations were >0.75 nM (Fig. 2). The cyan line marks the trajectory seeding depth which mimics a neutrally-buoyant plume. Bathymetry along 54°S (to match station OOI) is shown. Note the colorbar scale is different for **C** compared to **A** and **B**. **D** An east-west transect of excess Helium (xs^3He) at 54°S as an indicator of hydrothermal influence from the Jenkins et al. (2019) dataset⁵².

Trajectory estimates strongly supported a westerly source region with no influence from northerly ridge systems (Table 1). The SEPR region is identified as the most likely source for our observed signal. Forward-tracking simulations from the SEPR resulted in the greatest percentage of trajectories (9%) crossing within a 0.5° area around OOI at a depth coincident with the observed Fe and Mn enrichment compared to other release sites (Figure 3C; blue line). Similarly, in the backward-tracking simulations, the greatest percentage of trajectories (21%) released from OOI passed within the SEPR source region (Table 1). In an oceanographic context, these percentages can be thought of as demonstrating the strength and coherency of transport pathways within the wider ocean circulation between the source regions and OOI i.e. the greater the percentage the more dominant the pathway. The SEPR also had the shortest median transit timescales to/from OOI (10-12 years). Further west, the backward-tracking simulations indicate that 8-20% of trajectories starting at OOI intersect with the PAR ridge systems with a median transit time of 13-14 years. However, the peak in the trajectory signal propagated from the PAR regions were deeper than the observed Fe and Mn peaks at OOI, especially for PARS (Figure S3H). Our transit time estimates from the SEPR and PAR are at the lower end of estimated hydrothermal dFe residence times of 9-50 years^{39,42}.

The NEPR makes a minor contribution in both forward and backward trajectories over 20 years (0.3-1.3% of trajectories to/from OOI), with trajectories exhibiting longer median transit times to reach OOI (14-18 years), despite being much closer in proximity to OOI than the PARS site which made the second largest contribution (Fig. 1; Table 1). Similarly, trajectories from the Chile Rise did not intersect with the OOI site within 20 years.

Our simulations indicate minimal exchange between waters north and south of 45°S in the MAP, likely due to the South Pacific Current, which has diverging pathways above and below 40-43°S^{57,64}. This interpretation is supported by a model validation between the NEMO model used for the trajectory simulations and the Estimating the Circulation and Climate of the Ocean (ECCO) model state estimate^{65,66} (Figure S5). Both showed that the dominant currents at OOI originate from the west with weaker currents north of 45°S. Overall, the trajectory simulations indicated that the observed OOI trace metal plume originates from a ridge to the west of OOI, which is consistent with our understanding of the fast-moving ACC and weak currents in the northern MAP⁶⁷. Therefore, the strong xs³He signal to the north in the MAP region (Fig. S3A) should not be interpreted as traversing southwards towards OOI. Our results indicate that the xs³He signal observed at OOI has most likely traversed eastwards from the SEPR and/or from along the PAR (Fig. 3D). The PARS/N trajectory simulations highlight a pathway for potential hydrothermal transport along the PAR, that tracks northwards up to the SEPR and then eastwards towards the OOI site (Fig. S4E, G). Thus, it is possible we observed the amalgamation of trace metal inputs from multiple vent sites along the PAR and SEPR at the OOI site and along the transect, rather than a discrete single vent signal.

Systematic surveying for hydrothermal activity is lacking for the majority of the southern EPR and PAR systems⁶⁸. However, it is expected that the ridge system is hydrothermally active as multiple lines of evidence suggest that hydrothermal venting is common. Metalliferous sediments (enriched in Fe and Mn compared to aluminium), formed by precipitation of Fe and Mn from hydrothermal fluids, are

found along these ridge systems⁶⁹. Additionally, the magmatic budget hypothesis⁶⁸ predicts that variability in magma supply is the primary control on the large-scale hydrothermal distribution pattern along spreading ridges and is supported by a linear relationship between spreading rate and frequency of vent fields. Extrapolation of this relationship has been used to estimate a total of ~200-300 undiscovered vent fields along the SEPR and PAR with an average distance between vent fields along the SEPR of 25-30 km⁶⁸. Indeed, high resolution optical and redox sensor measurements made along 1470 km of intermediate and fast spreading mid-ocean ridge suggest that the frequency of vent sites is 3 to 6-fold higher than current observations (Fig. 1A), with a mean discharge spacing of 3-20 km⁷⁰.

Similarly, evidence from observational and modelling studies exists for the long-range transport of chemical signatures from these ridge systems. For example, sections of the PAR (south of 55°S) were identified as the likely source region of a ³He anomaly found on the neutral density surface $\gamma_n = 28.2$ kg m⁻³, indicative of active venting³³. Modelling dFe hydrothermal vent input as a function of ridge spreading rate found good agreement with observed dFe anomalies in the abyssal SO, with some of the highest rates of hydrothermal Fe input in the Pacific sector along the PAR and SEPR³⁹. Similarly, a global ocean modelling simulation of Mn predicted strong input from the SEPR which produced a dMn anomaly that extends to the location of our transect¹².

2.3 Could hydrothermal iron and manganese from southeast Pacific vents fuel Southern Ocean primary production?

The potential for hydrothermal Fe and Mn to fuel primary production depends on the balance between Fe and Mn residence times and the ventilation timescale of hydrothermal plume-influenced waters. A transit time of 99 ± 18 years for the shoaling of deep waters to the SO surface has been estimated using a global ³He mass balance model, in which ³He predominantly enters into the SO via deep South Eastern Pacific waters⁴⁶. Deep ocean re-exposure timescales of a few centuries have also

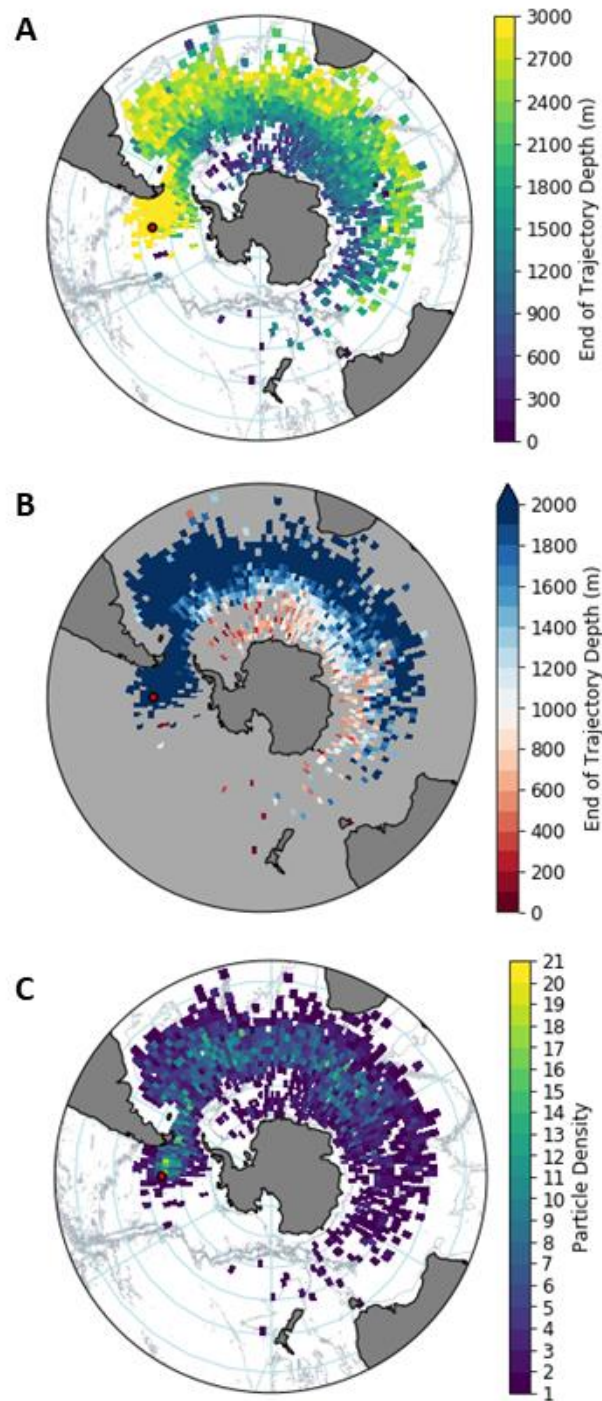
been calculated using a low horizontal resolution (2°) global steady-state ocean circulation inverse model⁴³. These ventilation timescales are likely incompatible with the notion that Fe and Mn from southeast Pacific vents could sustain significant amounts of Southern Ocean productivity when compared with estimated seawater residence times for Fe and Mn. Indeed, coupling a mechanistic Fe model, where hydrothermal input is estimated from a fixed Fe:³He ratio, with an ocean inverse circulation model allows for scavenging processes to effectively trap hydrothermal Fe in the deep ocean⁴⁰.

However, uncertainty around the magnitude of hydrothermal Fe input from SO ridge systems, and accounting for mesoscale processes when estimating ventilation timescales, may in fact allow for rapid transport of hydrothermal Fe and Mn to upper ocean waters. An inverse modelling approach reduces the magnitude of ³He input from SO ridge systems relative to a spreading rate model approach. A spreading rate model estimates ³He input as a function of ridge spreading rate, and likewise assigns an Fe:³He ratio to estimate a hydrothermal Fe flux³⁹. Significantly, the inverse model approach does not replicate the magnitude of an observed SO hydrothermal from the GEOTRACES GS01 section South of Tasmania³⁹. A consequence of the spatial redistribution of hydrothermal Fe input away from the SO vent sites by the inverse modelling approach is a reduction in the estimated amount of hydrothermal Fe reaching the upper 250 m of the ocean by 4-5-fold relative to the spreading rate model⁴⁰. It is also possible that previous studies may be over-estimating ventilation times due to their coarse resolution. Mesoscale (10-100 km) processes are important conduits for vertical mixing in the SO^{44,45}. Using an eddy-resolving Lagrangian particle tracking model transit times of 17-90 years were estimated for CDW (originating from 30°S between 1000-4000 m) to upwell to the SO mixed layer^{44,45}. Importantly, transit time estimates decrease as model resolution becomes finer^{44,45} with the shorter 17 year timescale estimated using a 0.1 degree eddy-resolving model. This highlights that accounting for mesoscale eddies is important for estimates of timescales for SO upwelling⁴⁵.

To investigate the potential fate of the observed dFe and dMn signals, we continued to forward-track trajectories that passed through our cruise transect at depths of the observed trace metal peak (2000-4000 m; Fig. 4). We thus estimated the proportion of trajectories which shoal to depths coincident with mixed layer depths associated with SO winter mixing, the key seasonal supply mechanism of micronutrients to SO surface waters³⁵. 83% of the trajectories passing through the cruise transect between 2000-4000m continued east through Drake Passage and then flowed northward away from the polar front ($\sim 60^\circ\text{S}$) into deep water masses (Fig. 4A; median depth 2087 m), and so are unlikely to supply hydrothermal Fe and Mn to the SO mixed layer. However, trajectories which pass through Drake Passage and traverse pathways south of 60°S (17%) tended to shoal in the water column by the end of the 20-year simulation (median depth 1043 m). Of the 17% of trajectories that passed south of 60°S , 10% (i.e., 1.7% of total trajectories) reached depths shallower than 600 m, a proxy for the winter maximum mixed layer depth in deep mixing regions of the SO⁷¹, while 31% (i.e. 5.3% of total) reached shallower than 1000 m, the maximum observed winter mixed layer depth⁷¹.

Our simulated trajectories thus indicate pathways from the observed deep southeast Pacific sector of the SO to the SO mixed layer within 20 years. Furthermore, the number of trajectories south of 60°S reaching winter mixing depths are likely to continue to increase beyond the temporal limit of our simulations (20 years). As discussed above, resolving mesoscale features in high-resolution models, as in our study (0.083° horizontal resolution), results in SO ventilation timescale estimates (within 20 years) that allow for hydrothermal Fe and Mn from SO vents to reach SO mixed layer depths within Fe and Mn residences times (5-50 years)⁴². Moreover, the effects of submesoscale mixing and dispersion, which will influence the transport and shoaling rates of dissolved constituents, are not resolved in the physical model driving our trajectory calculations but could further shorten ventilation timescales⁷². Trajectory modelling offers an alternate approach to identifying hydrothermal source regions and ventilation pathways and timescales, which may be more tractable for localised studies. It remains challenging to

isolate what drives the differences between Fe supply from different modelling approaches^{39,40} and ventilation timescales from high-resolution studies (<20 years)^{44,45}, compared to coarse-resolution or global inventory studies (~100 years)^{43,46} discussed above, as several factors change in tandem. The significance of transport pathways to the mixed layer must ultimately depend on the residence times of hydrothermal Fe and Mn being comparable or longer than the ventilation timescales we predict, as well as the consistency and stability of hydrothermal Fe and Mn inputs, both of which remain poorly constrained.



363

364 **Figure 4.** Indication of trajectory locations at the end of the 20 years simulation from the source regions.

365 **A** Trajectory depth and location at 20 years and B the depths presented as above (red) and below (blue)

366 the maximum winter MLD in the SO (1000m) and **C** Trajectory density at 20 years. OOI is shown by the
367 red marker. Note that only trajectories that passed within the cruise transect (OOI to 60°S) and the
368 observed hydrothermal signal depth range (2000-4000 m) are shown.

3.0 Conclusion

We identify potential pathways for Fe and Mn from SO hydrothermal vents to reach the SO mixed layer. Enhanced Fe and Mn concentrations were observed between 2000-4000 m depths within the southeast Pacific sector of the SO. The observed trace metal enrichment most likely originated from the South East Pacific Rise (south of 30°S). An origin further westward, such as from the Pacific Antarctic Ridge, was also possible. We further identified pathways for rapid (< 20 years) transport of water parcels enriched in hydrothermal Fe and Mn, from vents located within the understudied Pacific sector of the SO, to SO winter mixed layer depths. Consensus on the role of deep ocean hydrothermal trace metal inputs in fuelling upper ocean primary production has not yet been reached, with modelling studies disagreeing on the importance of SO vent systems for supplying hydrothermal Fe supply to the wider SO euphotic zone^{39,40}. However, we conclude that due to the vigorous action of the ACC, Pacific sector SO hydrothermal inputs provide the potential for sustained input of Fe and Mn to the euphotic zone south of the Antarctic Polar Front and far downstream of the deep ocean vent sites, potentially fuelling productivity in remote areas of the SO. Given the existence of ridge systems throughout the SO, it is likely that other similar pathways exist that rapidly transport Fe and Mn from vent sites to the SO euphotic zone.

Methods

Trace Metal and Macronutrient Methods

Sampling was conducted during December 2019 and January 2020 on board the *R.R.S. Discovery* along a transect in the eastern Pacific sector of the SO (Fig.1). All trace metal samples were collected following GEOTRACES protocols⁷³.

Briefly, dissolved Fe (0.2 μ m filtered) and TdFe (unfiltered) were analyzed using flow injection with chemiluminescence detection, after spiking with hydrogen peroxide⁷⁴, in a clean laboratory at the University of Plymouth. The mean limit of detection was 0.012 ± 0.009 nM and limit of quantification 0.038 ± 0.026 nM (n=54). Additional seawater samples collected in >1 L volumes, and acidified for > 6 months, were used as in-house quality control materials as a measure of precision and were analysed every 10 samples. 4 in-house quality control materials were analysed; #1 0.17 ± 0.01 nM (n=45), #2 0.22 ± 0.04 nM (n=54), #3 0.26 ± 0.03 nM (n=124) and #4 0.19 ± 0.03 nM (n=70). GEOTRACES GSP and SFe D1 and S consensus values were analysed to determine accuracy, consensus values are (GSP 0.16 ± 0.05 nM, D1 0.65 ± 0.04 nM, S 0.10 ± 0.01 nM), which compared well to values determined (GSP 0.20 ± 0.020 nM, D1 0.66 ± 0.066 , S 0.10 ± 0.01 nM). The authors have previously published bottom up and top-down combined analytical uncertainty estimates (u_c 5-10 % (k=1)) for this technique^{75,76}.

A subset of samples from the northern, middle, and southern stations were chosen for further trace metal analysis. Dissolved Mn (0.2 μ m filtered) concentration was determined using a standard addition method with off-line pre-concentration and subsequent high resolution ICP-MS²⁹ at the National Oceanography Centre, Southampton, UK. The mean limit of detection was 0.011 ± 0.004 nM (n=3). Consensus values for SFe S (0.812 ± 0.062 nM) and D2 (0.360 ± 0.051 nM) reference material compared well with our measured values (0.769 ± 0.059 nM and 0.372 ± 0.030 nM, respectively).

408 *Inorganic Nutrient Analysis*

409 Seawater samples were analysed for nitrate (determined as nitrate + nitrite; $\text{NO}_3^- + \text{NO}_2^-$), silicate (SiO_4^{4-}),
410 nitrite (NO_2^-) and phosphate (PO_4^{3-}). Samples were drawn from Niskin bottles into rinsed 15 mL
411 centrifuge tubes. Colorimetric analysis was undertaken within 24 hours of the samples being taken and
412 performed using SEAL QuAatro 39 segmented flow autoanalyser⁷⁷. Two sets of certified reference
413 materials (CRM Lots CJ and CB, KANSO, Japan) were determined at a start and the end of each sample
414 run to ensure accuracy. Depending on an analysis run, the detection limits for each parameter ranged as
415 follows: 0.02-0.2 μM for nitrate + nitrite, 0.02-0.15 μM for silicate, 0.01-0.033 μM for nitrite, and 0.002-
416 0.019 μM for phosphate.

417

418 *Temperature and Salinity Calibration*

419 Trace-metal clean samples were taken with a titanium frame Conductivity Temperature Depth (CTD) fitted
420 with 10 L Niskin bottles and a SBE 9 plus underway unit. Conductivity (and calculated salinity) data were
421 calibrated against samples taken from each cast and run on an Autosal 8400B salinometer. The salinity
422 was accurate to within ± 0.004 . There was no SBE35 thermometer fitted on the titanium frame but
423 comparison with co-located calibrated stainless steel casts showed good agreement and data is accurate
424 to better than $\pm 0.005^\circ\text{C}$

425

426 *Excess Helium Calculations*

427 ^3He is a primordial substance trapped in the mantle during planetary formation. Ratios of $^3\text{He}/^4\text{He}$ in
428 excess of atmospheric values indicate a contribution from the mantle, therefore ^3He can be used to
429 identify ocean waters that have been influenced by hydrothermal activity. Excess ^3He is the approximate

430 measure of non-atmospheric ^3He over saturation, we followed the approach outlined in Resing et al.
431 (2015)²³:

432 $^3\text{He}_{\text{XS}} = (\delta^3\text{He} - \delta^{3*}\text{He}) / 100 \times \text{C}[\text{He}] \times 1.384 \times 10^{-6}$

433 where $\delta^3\text{He} = 100 \times (\text{Rx}/\text{Ra} - 1) \times 100\%$, Rx and Ra are the $^3\text{He}/^4\text{He}$ ratios of the sample and air ($1.384 \times$
434 10^{-6}), respectively. $\delta^{3*}\text{He}$ is the helium isotope ratio anomaly in solubility equilibrium with the
435 atmosphere.

436

437 *Trajectory Modelling*

438 To identify the potential source of the observed hydrothermal Fe and Mn signal we focus on regions
439 along the Chile Rise (CR), East Pacific Rise (NEPR and SEPR) and Pacific-Antarctic Ridge (PARN and PARS),
440 with regions of suspected hydrothermal activity shown in Fig. 1A (triangles).

441 Trajectories were used to identify the region(s) that were most likely to be the source of the deep water
442 hydrothermal iron signal. Trajectories were tracked forwards from possible vent sites which may act as a
443 source, and backwards from the OOI sustained observatory site, where enrichments in midwater
444 micronutrient concentrations were observed. Trajectories do not represent quantities or concentrations
445 of dFe or dMn. The velocity components used to calculate trajectories do not represent submesoscale
446 mixing or dispersion processes⁶², which may affect the pathway of dissolved constituents in the ocean.

447 We estimated 20-year trajectories using ‘parcels’ (version 2.2.0; <https://oceanparcels.org/>⁶²). Parcels
448 was applied to the NEMO eddy-resolving general circulation model (ORCA0083-N06⁶³). Model output at
449 $1/12^\circ$ horizontal resolution from 1992-2011 was used as a 20-year climatology of the hydrodynamic flow
450 field. NEMO was coupled to a sea-ice model (LIM2⁷⁸) and was forced with historical atmospheric
451 reanalysis (Drakkar Forcing Set 5.2⁷⁹). The simulations were carried out using 3D Runge-Kutta fourth

order (RK4) timestep integration as the advection scheme with a timestep of 1 day to estimate the trajectories⁸⁰. The trajectory position was exported every 5 days.

Applying 'parcels' to velocity components on a C grid whilst using an RK4 advection scheme, with a Lagrangian timestep of 1 day, can lead to trajectories 'overshooting' the ocean grid cells into bathymetry. To reduce the occurrences of particles travelling out of bounds we added a criterion that returned such trajectories to 10 m above the seafloor⁸¹. This criterion was applied to 4.7% of the total timesteps in the backwards-tracked trajectories and for an average of 22.9% of timesteps for the forward-tracked trajectories, due to the trajectory start locations being in close proximity to seafloor topography, i.e. vent sites along ocean ridges.

Forward-tracking Trajectories

Six potential source regions were identified (Fig. 1A, triangles) and referred to as the East Chile Rise (ECR), West Chile Rise (WCR), Easter Microplate (EM), North East Pacific Rise (NEPR), South East Pacific Rise (SEPR) and the Pacific Antarctic Ridge (PAR; Table S2). Trajectories were initialised over a 0.5° grid around each potential source location at 100 m intervals between 2000-4000 m. 2000 trajectories were initiated per depth. In regions of bathymetry shallower than 4000 m, fewer trajectories were tracked. All calculations were normalised to the number of successfully tracked trajectories (Table S2) that were within a plume. We define the plume by the deepest depth of successful trajectories initialisation within each 0.5° release area, to mimic the deepest possible vent depth, up to 500 m shallower in the water column. Trajectories that crossed within a 0.5° area around the OOI site were isolated to estimate the dilution percentage of trajectories from the source regions (trajectory start locations) to OOI (Table S3). The EM had no trajectories passing near the OOI site and was not included in the analysis (Table S2).

Backward-tracking Trajectories

474 To complement the forward-tracking we initiated trajectories throughout the water column at OOI to
475 coincide with the depths at which the dFe and dMn signal was observed. Trajectories were initialised
476 over a 0.5° grid around the OOI sustained observatory site every 50m between 2000-4000 m. 1000
477 trajectories were released per depth and tracked backwards in time for 20 years (2011 to 1992; Table
478 S2).

479 We defined 5 potential hydrothermal signal source regions along the Pacific Antarctic Ridge, East Pacific
480 Rise and the Chile Rise to further evaluate where the iron signal was most likely to originate from – ECR
481 and WCR as CR, NEPR, SEPR, Pacific Antarctic Ridge North (PARN), and Pacific Antarctic Ridge South
482 (PARS; Table S4). Trajectories were only classed as originating from that source region if they entered at
483 depths within a range of 500 m above the deepest possible vent height within each release area to
484 mimic a plume^{82,83}. For PARN, which had no specific vent release site for the forward tracking simulation,
485 a vent depth of 2500 m was chosen by examining the depths of the topography within the PARN area as
486 a histogram to identify the ridge depths. The fraction of trajectories passing into each source region is
487 presented as the dilution percentage (Table 1).

488

489 **Acknowledgements**

490 A.J.B., C.A.B., N.J.W., K.P., H.J.V., A.M, S.J.U., C.M.M., S.O. and A.P.M. were supported by Natural
491 Environment Research Council (NERC) funding for the CUSTARD project (NE/P021247/2; NE/P021336/1;
492 NE/P021328/1). I.T. was supported by the ARIES DTP (NE/V009877/1). We would like to thank the NMF
493 technicians and the RRS Discovery ship's captain, officers crew for their support during DY111. We
494 would like to acknowledge and thank the parcels (<https://oceanparcels.org/>) developers, the JASMIN
495 service (<https://jasmin.ac.uk/>), the ECCO Consortium and Ocean Data View developers
496 (<https://odv.awi.de>) for their efforts. We would like to thank Alessandro Tagliabue and William Jenkins
497 for their useful and informative discussions around our research.

498

499 **Data Statement**

500 Lagrangian trajectories from the tracking using parcels are available at Zenodo
501 (DOI:10.5281/zenodo.8153763). The NEMO model velocity components used to force parcels can be
502 found on JASMIN (<https://www.ceda.ac.uk/services/jasmin/>). The micronutrient data has been
503 submitted to the British Oceanographic Data Centre (DOI: 10.5285/0c7760cc-98fb-5861-e063-
504 6c86abc0a998). The macronutrient data is available from the British Oceanographic Data Centre.

References

1. Boyd, P. W., Arrigo, K. R., Strzepek, R. & van Dijken, G. L. Mapping phytoplankton iron utilization: Insights into Southern Ocean supply mechanisms. *J. Geophys. Res. Ocean.* **117**, 1–18 (2012).
2. Balaguer, J., Koch, F., Hassler, C. & Trimborn, S. Iron and manganese co-limit the growth of two phytoplankton groups dominant at two locations of the Drake Passage. *Commun. Biol.* **5**, 207 (2022).
3. MacGilchrist, G. A. *et al.* Reframing the carbon cycle of the subpolar Southern Ocean. *Sci. Adv.* **5**, 1–9 (2019).
4. Dunne, J. P., Sarmiento, J. L. & Gnanadesikan, A. A synthesis of global particle export from the surface ocean and cycling through the ocean interior and on the seafloor. *Global Biogeochem. Cycles* **21**, 1–16 (2007).
5. Moore, C. M. *et al.* Processes and patterns of oceanic nutrient limitation. *Nat. Geosci.* **6**, 701–710 (2013).
6. Tagliabue, A. *et al.* The integral role of iron in ocean biogeochemistry. *Nature* **543**, 51–59 (2017).
7. Browning, T. J. & Moore, C. M. Global analysis of ocean phytoplankton nutrient limitation reveals high prevalence of co-limitation. *Nat. Commun.* **14**, 1–12 (2023).
8. Browning, T. J., Achterberg, E. P., Engel, A. & Mawji, E. Manganese co-limitation of phytoplankton growth and major nutrient drawdown in the Southern Ocean. *Nat. Commun.* **12**, 884 (2021).
9. Hawco, N. J., Tagliabue, A. & Twining, B. S. Manganese Limitation of Phytoplankton Physiology and Productivity in the Southern Ocean. *Global Biogeochem. Cycles* **36**, (2022).
10. Wyatt, N. J. *et al.* Phytoplankton responses to dust addition in the Fe–Mn co-limited eastern

- 526 Pacific sub-Antarctic differ by source region. *Proc. Natl. Acad. Sci.* **120**, 2017 (2023).
- 527 11. Hayes, C. T. *et al.* Replacement Times of a Spectrum of Elements in the North Atlantic Based on
528 Thorium Supply. *Global Biogeochem. Cycles* **32**, 1294–1311 (2018).
- 529 12. van Hulten, M. *et al.* Manganese in the west Atlantic Ocean in the context of the first global
530 ocean circulation model of manganese. *Biogeosciences* **14**, 1123–1152 (2017).
- 531 13. Pollard, R., Sanders, R., Lucas, M. & Statham, P. The Crozet Natural Iron Bloom and Export
532 Experiment (CROZEX). *Deep. Res. Part II Top. Stud. Oceanogr.* **54**, 1905–1914 (2007).
- 533 14. Moore, C. M. *et al.* Iron-light interactions during the CROZet natural iron bloom and EXport
534 experiment (CROZEX) I: Phytoplankton growth and photophysiology. *Deep. Res. Part II Top. Stud.*
535 *Oceanogr.* **54**, 2045–2065 (2007).
- 536 15. McGillicuddy, D. J. *et al.* Iron supply and demand in an Antarctic shelf ecosystem. *Geophys. Res.*
537 *Lett.* **42**, 8088–8097 (2015).
- 538 16. Middag, R., de Baar, H. J. W., Laan, P., Cai, P. H. & van Ooijen, J. C. Dissolved manganese in the
539 Atlantic sector of the Southern Ocean. *Deep Sea Res. Part II Top. Stud. Oceanogr.* **58**, 2661–2677
540 (2011).
- 541 17. Gerringa, L. J. A. *et al.* Sources of iron in the Ross Sea Polynya in early summer. *Mar. Chem.* **177**,
542 447–459 (2015).
- 543 18. Sholkovitz, E. R., Sedwick, P. N. & Church, T. M. Influence of anthropogenic combustion emissions
544 on the deposition of soluble aerosol iron to the ocean: Empirical estimates for island sites in the
545 North Atlantic. *Geochim. Cosmochim. Acta* **73**, 3981–4003 (2009).
- 546 19. Mahowald, N. M. *et al.* Atmospheric iron deposition: Global distribution, variability, and human

- 547 perturbations. *Ann. Rev. Mar. Sci.* **1**, 245–278 (2009).
- 548 20. Findlay, A. J. *et al.* Iron and sulfide nanoparticle formation and transport in nascent hydrothermal
549 vent plumes. *Nat. Commun.* **10**, 1597 (2019).
- 550 21. Tagliabue, A. & Resing, J. Impact of hydrothermalism on the ocean iron cycle. *Philos. Trans. R.*
551 *Soc. A Math. Phys. Eng. Sci.* **374**, 20150291 (2016).
- 552 22. German, C. R., Campbell, A. C. & Edmond, J. M. Hydrothermal scavenging at the Mid-Atlantic
553 Ridge: Modification of trace element dissolved fluxes. *Earth Planet. Sci. Lett.* **107**, 101–114
554 (1991).
- 555 23. Resing, J. A. *et al.* Basin-scale transport of hydrothermal dissolved metals across the South Pacific
556 Ocean. *Nature* **523**, 200–203 (2015).
- 557 24. Fitzsimmons, J. N., Boyle, E. A. & Jenkins, W. J. Distal transport of dissolved hydrothermal iron in
558 the deep South Pacific Ocean. *Proc. Natl. Acad. Sci.* **111**, 16654–16661 (2014).
- 559 25. Wu, J., Wells, M. L. & Rember, R. Dissolved iron anomaly in the deep tropical–subtropical Pacific:
560 Evidence for long-range transport of hydrothermal iron. *Geochim. Cosmochim. Acta* **75**, 460–468
561 (2011).
- 562 26. Tagliabue, A. *et al.* Hydrothermal contribution to the oceanic dissolved iron inventory. *Nat.*
563 *Geosci.* **3**, 252–256 (2010).
- 564 27. Yücel, M., Gartman, A., Chan, C. S. & Luther, G. W. Hydrothermal vents as a kinetically stable
565 source of iron-sulphide-bearing nanoparticles to the ocean. *Nat. Geosci.* **4**, 367–371 (2011).
- 566 28. Findlay, A. J., Gartman, A., Shaw, T. J. & Luther, G. W. Trace metal concentration and partitioning
567 in the first 1.5 m of hydrothermal vent plumes along the Mid-Atlantic Ridge: TAG, Snakepit, and

- 568 Rainbow. *Chem. Geol.* **412**, 117–131 (2015).
- 569 29. Lough, A. J. M. *et al.* Soluble iron conservation and colloidal iron dynamics in a hydrothermal
570 plume. *Chem. Geol.* **511**, 225–237 (2019).
- 571 30. Sander, S. G. & Koschinsky, A. Metal flux from hydrothermal vents increased by organic
572 complexation. *Nat. Geosci.* **4**, 145–150 (2011).
- 573 31. Toner, B. M. *et al.* Preservation of iron(II) by carbon-rich matrices in a hydrothermal plume. *Nat.*
574 *Geosci.* **2**, 197–201 (2009).
- 575 32. Lupton, J. Hydrothermal helium plumes in the Pacific Ocean. *J. Geophys. Res. Ocean.* **103**, 15853–
576 15868 (1998).
- 577 33. Winckler, G., Newton, R., Schlosser, P. & Crone, T. J. Mantle helium reveals Southern Ocean
578 hydrothermal venting. *Geophys. Res. Lett.* **37**, 1–5 (2010).
- 579 34. Toggweiler, J. R. & Samuels, B. On the ocean’s large-scale circulation near the limit of no vertical
580 mixing. *J. Phys. Oceanogr.* **28**, 1832–1852 (1998).
- 581 35. Tagliabue, A. *et al.* Surface-water iron supplies in the Southern Ocean sustained by deep winter
582 mixing. *Nat. Geosci.* **7**, 314–320 (2014).
- 583 36. Schine, C. *et al.* Massive Bloom Fed by Elevated Iron of Possible Hydrothermal Origin in the
584 Pacific Sector of the Southern Ocean. *2020 Ocean Sci. Meet.* CT23A-03 (2020)
585 doi:10.1038/s41467-021-21339-5.
- 586 37. Ardyna, M. *et al.* Hydrothermal vents trigger massive phytoplankton blooms in the Southern
587 Ocean. *Nat. Commun.* **10**, 1–8 (2019).
- 588 38. Bonnet, S. *et al.* Natural iron fertilization by shallow hydrothermal sources fuels diazotroph

589 blooms in the ocean. *Science* (80-.). **380**, 812–817 (2023).

590 39. Tagliabue, A. *et al.* Constraining the Contribution of Hydrothermal Iron to Southern Ocean Export
591 Production Using Deep Ocean Iron Observations. *Front. Mar. Sci.* **9**, 1–10 (2022).

592 40. Roshan, S., DeVries, T., Wu, J., John, S. & Weber, T. Reversible scavenging traps hydrothermal
593 iron in the deep ocean. *Earth Planet. Sci. Lett.* **542**, 116297 (2020).

594 41. Carazzo, G., Jellinek, A. M. & Turchyn, A. V. The remarkable longevity of submarine plumes:
595 Implications for the hydrothermal input of iron to the deep-ocean. *Earth Planet. Sci. Lett.* **382**,
596 66–76 (2013).

597 42. Kipp, L. E. *et al.* Radium isotopes as tracers of hydrothermal inputs and neutrally buoyant plume
598 dynamics in the deep ocean. *Mar. Chem.* **201**, 51–65 (2018).

599 43. DeVries, T. & Holzer, M. Radiocarbon and Helium Isotope Constraints on Deep Ocean Ventilation
600 and Mantle-3He Sources. *J. Geophys. Res. Ocean.* **124**, 3036–3057 (2019).

601 44. Tamsitt, V. *et al.* Spiraling pathways of global deep waters to the surface of the Southern Ocean.
602 *Nat. Commun.* **8**, 1–10 (2017).

603 45. Drake, H. F. *et al.* Lagrangian Timescales of Southern Ocean Upwelling in a Hierarchy of Model
604 Resolutions. *Geophys. Res. Lett.* **45**, 891–898 (2018).

605 46. Jenkins, W. J. Using Excess 3He to Estimate Southern Ocean Upwelling Time Scales. *Geophys. Res.*
606 *Lett.* **47**, 1–10 (2020).

607 47. de Baar, H. J. W. *et al.* Low dissolved Fe and the absence of diatom blooms in remote Pacific
608 waters of the Southern Ocean. *Mar. Chem.* **66**, 1–34 (1999).

609 48. Gourain, A. *et al.* Inputs and processes affecting the distribution of particulate iron in the North

- 610 Atlantic along the GEOVIDE (GEOTRACES GA01) section. *Biogeosciences* **16**, 1563–1582 (2019).
- 611 49. Beaulieu, S. E., Baker, E. T., German, C. R. & Maffei, A. An authoritative global database for active
612 submarine hydrothermal vent fields. *Geochemistry, Geophys. Geosystems* **14**, 4892–4905 (2013).
- 613 50. Kawabe, M. & Fujio, S. Pacific ocean circulation based on observation. *J. Oceanogr.* **66**, 389–403
614 (2010).
- 615 51. Well, R., Roether, W. & Stevens, D. P. An additional deep-water mass in Drake Passage as
616 revealed by ^3He data. *Deep. Res. Part I Oceanogr. Res. Pap.* **50**, 1079–1098 (2003).
- 617 52. Jenkins, W. J. *et al.* A comprehensive global oceanic dataset of helium isotope and tritium
618 measurements. *Earth Syst. Sci. Data* **11**, 441–454 (2019).
- 619 53. Zheng, L., Minami, T., Takano, S. & Sohrin, Y. Distributions of aluminum, manganese, cobalt, and
620 lead in the western South Pacific: Interplay between the South and North Pacific. *Geochim.*
621 *Cosmochim. Acta* **338**, 105–120 (2022).
- 622 54. Gamo, T. *et al.* Chemical characteristics of hydrothermal fluids from the TAG Mound of the Mid-
623 Atlantic Ridge in August 1994: Implications for spatial and temporal variability of hydrothermal
624 activity. *Geophys. Res. Lett.* **23**, 3483–3486 (1996).
- 625 55. Fitzsimmons, J. N. *et al.* Iron persistence in a distal hydrothermal plume supported by dissolved–
626 particulate exchange. *Nat. Geosci.* **10**, 195–201 (2017).
- 627 56. Tagliabue, A. *et al.* The interplay between regeneration and scavenging fluxes drives ocean iron
628 cycling. *Nat. Commun.* **10**, 1–8 (2019).
- 629 57. Reid, J. L. On the total geostrophic circulation of the South Pacific Ocean: Flow patterns, tracers
630 and transports. *Prog. Oceanogr.* **16**, 1–61 (1986).

- 631 58. Shaffer, G., Salinas, S., Pizarro, O., Vega, A. & Hormazabal, S. Currents in the deep ocean off Chile
632 (30°S). *Deep Sea Res. Part I Oceanogr. Res. Pap.* **42**, 425–436 (1995).
- 633 59. Baker, E. T. & Massoth, G. J. Characteristics of hydrothermal plumes from two vent fields on the
634 Juan de Fuca Ridge, northeast Pacific Ocean. *Earth Planet. Sci. Lett.* **85**, 59–73 (1987).
- 635 60. Klinkhammer, G., Rona, P., Greaves, M. & Elderfield, H. Hydrothermal manganese plumes in the
636 Mid-Atlantic Ridge rift valley. *Nature* **314**, 727–731 (1985).
- 637 61. Lupton, J. E. & Craig, H. A major helium-3 source at 15°S on the east Pacific rise. *Science* (80-.).
638 **214**, 13–18 (1981).
- 639 62. Delandmeter, P. & Van Sebille, E. The Parcels v2.0 Lagrangian framework: New field interpolation
640 schemes. *Geosci. Model Dev.* **12**, 3571–3584 (2019).
- 641 63. Madec, G. & Team, N. *NEMO ocean engine*. (2016).
- 642 64. Strub, P. T., James, C., Montecino, V., Rutllant, J. A. & Blanco, J. L. Ocean circulation along the
643 southern Chile transition region (38°–46°S): Mean, seasonal and interannual variability, with a
644 focus on 2014–2016. *Prog. Oceanogr.* **172**, 159–198 (2019).
- 645 65. Forget, G. *et al.* ECCO version 4: an integrated framework for non-linear inverse modeling and
646 global ocean state estimation. *Geosci. Model Dev.* **8**, 3071–3104 (2015).
- 647 66. ECCO Consortium, Fukumori, I., Wang, O., Fenty, I., Forget, G., Heimbach, P., & Ponte, R. M. ECCO
648 Central Estimate (Version 4 Release 4). <https://www.ecco-group.org/products-ECCO-V4r4.htm>.
- 649 67. Faure, V. & Speer, K. Deep circulation in the eastern south pacific ocean. *J. Mar. Res.* **70**, 748–778
650 (2012).
- 651 68. Beaulieu, S. E., Baker, E. T. & German, C. R. Where are the undiscovered hydrothermal vents on

- 652 oceanic spreading ridges? *Deep Sea Res. Part II Top. Stud. Oceanogr.* **121**, 202–212 (2015).
- 653 69. Boström, K., Peterson, M. N. A., Joensuu, O. & Fisher, D. E. Aluminum-poor ferromanganoan
654 sediments on active oceanic ridges. *J. Geophys. Res.* **74**, 3261–3270 (1969).
- 655 70. Baker, E. T. *et al.* How many vent fields? New estimates of vent field populations on ocean ridges
656 from precise mapping of hydrothermal discharge locations. *Earth Planet. Sci. Lett.* **449**, 186–196
657 (2016).
- 658 71. Buongiorno Nardelli, B. *et al.* Southern Ocean Mixed-Layer Seasonal and Interannual Variations
659 From Combined Satellite and In Situ Data. *J. Geophys. Res. Ocean.* **122**, 10042–10060 (2017).
- 660 72. Bachman, S. D. & Klocker, A. Interaction of jets and submesoscale dynamics leads to rapid ocean
661 ventilation. *J. Phys. Oceanogr.* **50**, 2873–2883 (2020).
- 662 73. Cutter, G. A. *et al.* Sampling and Sample-handling Protocols for GEOTRACES Cruises. (2010).
- 663 74. Birchill, A. J. *et al.* Seasonal iron depletion in temperate shelf seas. *Geophys. Res. Lett.* **44**, 8987–
664 8996 (2017).
- 665 75. Floor, G. H. *et al.* Combined uncertainty estimation for the determination of the dissolved iron
666 amount content in seawater using flow injection with chemiluminescence detection. *Limnol.*
667 *Oceanogr. Methods* **13**, 673–686 (2015).
- 668 76. Worsfold, P. J. *et al.* Estimating uncertainties in oceanographic trace element measurements.
669 *Front. Mar. Sci.* **6**, 1–9 (2019).
- 670 77. Grasshoff, K., Kremling, K. & Ehrhardt, M. *Methods of Seawater Analysis*. (Wiley, 1999).
671 doi:10.1002/9783527613984.
- 672 78. Bouillon, S., Morales Maqueda, M. Á., Legat, V. & Fichet, T. An elastic-viscous-plastic sea ice

673 model formulated on Arakawa B and C grids. *Ocean Model.* **27**, 174–184 (2009).

674 79. Brodeau, L., Barnier, B., Treguier, A. M., Penduff, T. & Gulev, S. An ERA40-based atmospheric
675 forcing for global ocean circulation models. *Ocean Model.* **31**, 88–104 (2010).

676 80. van Sebille, E. *et al.* Lagrangian ocean analysis: Fundamentals and practices. *Ocean Model.* **121**,
677 49–75 (2018).

678 81. Baker, C. A., Martin, A. P., Yool, A. & Popova, E. Biological carbon pump sequestration efficiency
679 in the North Atlantic: A leaky or a long-term sink? *Global Biogeochem. Cycles* (2022)
680 doi:10.1029/2021gb007286.

681 82. German, C. R. *et al.* Diverse styles of submarine venting on the ultraslow spreading Mid-Cayman
682 Rise. *Proc. Natl. Acad. Sci. U. S. A.* **107**, 14020–14025 (2010).

683 83. Baker, E. T. *et al.* Hydrothermal venting in magma deserts: The ultraslow-spreading Gakkel and
684 Southwest Indian Ridges. *Geochemistry, Geophys. Geosystems* **5**, 1–29 (2004).

685

686